Journal of Applied Physics

Time-dependent laser irradiation-induced kinetics of changes in linear–nonlinear optical properties of $Bi_{15}In_{20}Se_{65}$ thin films for IR applications

Cite as: J. Appl. Phys. **133**, 063104 (2023); https://doi.org/10.1063/5.0133479
Submitted: 03 November 2022 • Accepted: 29 January 2023 • Published Online: 14 February 2023

P. Priyadarshini, A. Parida, D. Alagarasan, et al.

AIP Publishing

Journal of Applied Physics ARTICLE scitation.org/journal/jap

Time-dependent laser irradiation-induced kinetics of changes in linear–nonlinear optical properties of $Bi_{15}In_{20}Se_{65}$ thin films for IR applications

Cite as: J. Appl. Phys. **133**, 063104 (2023); doi: 10.1063/5.0133479
Submitted: 3 November 2022 · Accepted: 29 January 2023 ·
Published Online: 14 February 2023

P. Priyadarshini,[1] A. Parida,[1] D. Alagarasan,[2,3] R. Ganesan,[2] and R. Naik[1,a)]

AFFILIATIONS

[1]Department of Engineering and Material Physics, ICT-IOC, Bhubaneswar 751013, India
[2]Department of Physics, Indian Institute of Science, Bengaluru 560012, India
[3]Department of Physics, Nitte Meenakshi Institute of Technology, Yelahanka, Bengaluru 560064, India

[a)]**Author to whom correspondence should be addressed:** ramakanta.naik@gmail.com

ABSTRACT

The current research depicts the laser irradiation-induced effect on the optoelectrical and structural properties of thermally evaporated $Bi_{15}In_{20}Se_{65}$ thin films with different exposure durations (0, 10, 20, 30, 60, and 90 min). The illumination effect under different lasing times leads to the retention of amorphous nature, indicating the short-range ordering inside the matrix. An improvement in the homogeneous and smooth texture of the film surface even after irradiation has been observed. However, significant optical changes have been noticed with different exposure durations. Transparency decreased with the exposure time, whereas an increment in the absorption coefficient with red shifting in the absorption edge was observed. Broad transparency and less absorption over the infrared region make these films promising for infrared optics such as temperature detection, energy management, monitoring, night vision, etc. Laser illumination allowed bond rearrangements that led to an increase in defect states over the forbidden gap regime and reduced the bandgap from 1.02 to 0.94 eV, confirming the photodarkening nature. This consequently enhanced the Urbach energy and electron–phonon interactions. Both extinction coefficient and refractive index enhanced with lasing duration, indicating an increment in the scattering centers with the lasing duration. The increase in the lasing time results in the increase of interband transitions, which might be due to the increase of carrier concentrations in the system. The non-linear susceptibility ($\chi^{(3)}$) and refractive indices showed enhancement with exposure duration. The observed non-linear refractive index (SI) is 20–30 times greater than silica. This reduction of E_g and enhancement in non-linearity improves the occurrence of two-photon absorption, signifying the potentiality for photonic devices. The hydrophilic nature of laser-irradiated films makes them suitable for applications such as self-cleaning, antifouling, and antifogging as coating materials.

I. INTRODUCTION

Recently, there has been much interest in the study of external energy-induced material characteristics from the standpoint of both basic physics and device technology. Several external energy inputs such as foreign elements doping,[1] ion irradiation,[2] laser irradiation,[3] and thermal annealing[4] impact on various properties of thin films, opening up new pathways for many applications in photonics and optoelectronic devices. Among them, laser-induced modifications in amorphous materials are considered an important aspect that includes a better understanding of the mechanism in amorphous materials and corresponding practical applications. Photo-created modifications in amorphous materials include irradiation of light excitation having energy near to the band energy of these materials, which leads to alterations of the amorphous matrix resulting in the structural rearrangement of lattices and changes in optical behavior.[5] Numerous photo-induced phenomena, such as photo-crystallization/amorphization, photo contraction/expansion, and photo dissolution of materials, result in an atomic level modification.[6] Photodarkening (PD) and photobleaching (PB) are the most commonly observed behaviors, depending on the red/blue shift of the optical absorption edge and a consequent change in the optical bandgap (E_g). The magnitude of PD and PB is mainly related to the composition and structure of materials. For example, the as-prepared $Ge_{29}Sb_8Se_{63}$ thin film showed fast PD

followed by a slow dominative PB process, while the same annealed film showed only PD behavior over prolonged irradiation.[7] Such verities of light-induced transformations in amorphous materials have potential applications in optoelectronics such as photonic switching and computing, optical memories, optoelectronic circuits, and photolithography.[8] The exposure of $Se_{58}Ge_{27}Pb_{15}$ and $Se_{58}Ge_{24}Pb_{18}$ thin films to laser irradiation resulted in a decrement in E_g, along with phase transformation, which is beneficial for optical recording media.[9]

In this regard, amorphous chalcogenide materials have received much attention and have been thoroughly studied due to their photo-induced intriguing modifications in various properties, such as large non-linearities, high refractive index, and excellent transparency over the infrared (IR) spectrum.[10,11] These materials were very responsive to photo-induced phenomena when irradiated with a laser source with photon energy (hν) equal to the band energy of the material, resulting in structural transformations, optical property changes, and so on. As a result, they are more appealing for use in integrated optics, absorption filters, imaging media, and a variety of other optical components. The laser-induced effect on Ge–Se–Bi thin films results in an increment in E_g, with PB behavior and showed the irreversible nature of optical properties, which might be applicable for optical and integrated optical elements.[12] Similarly, with different exposure times, the Nd:YAG laser (488 nm) irradiation-induced $Ge_1Se_{2.5}$ thin film showed an enhancement in the degree of crystallinity with a significant increase in non-linearity, which makes it suitable for non-linear optical potential devices and optical memory devices.[13] The Ge–Sb–Se film-based IR motherboard has been fabricated by using femtosecond laser micromachining, which showed an impactful reduction in the refractive index and E_g, while an increment in the absorption coefficient has been observed with laser power variation.[14] The laser irradiation effect on $As_{40}Se_{55}Bi_5$ thin films having lasing energy equal to band energy showed structural alteration along with the PD effect because of the change in the defect states over the band regime.[15] Thus, this study mainly focused on laser irradiation that induced various material properties with different exposure times.

The Bi–In–Se (V–III–VI) composition is considered an idealized chalcogenide semiconducting material with applications including non-linear optics, electrical switching, solar cells, photodetectors, and diodes.[16,17] Numerous investigations on this ternary Bi–In–Se system have been done with much attention for their fascinating optoelectronic properties, which lead to new positive and promising applications of multifunctional chalcogenide frameworks.[18,19] The compositional variation study on $Bi_xIn_{35-x}Se_{65}$ thin films revealed the phase transformation nature for a 15% Bi-doped film ($Bi_{15}In_{20}Se_{65}$) along with greater non-linear susceptibility and refractive index, compared to other films.[19] Previously, the investigation of the laser-induced structural and optical properties of the bilayer Bi/In_2Se_3 thin film revealed a phase transformation along with high tuning in optical-related parameters.[20] Additionally, the time evolution study of laser irradiation significantly affects the kinetics of changes in the film, which provides metastable and permanent optical changes. This plays a crucial point in understanding the basic mechanism and its technological applications. Thus, to expand the study on laser irradiation-induced tuning of various properties with a deeper understanding, the current study aims to analyze the irradiation-caused changes in various optical, structural, and morphological aspects due to exposure time variation.

The present study is focused on the investigation of the effects due to laser irradiation on different properties related to the structural, morphological, optical, and surface wettability of thermally evaporated $Bi_{15}In_{20}Se_{65}$ thin films at different exposure durations (0, 10, 20, 30, 60, and 90 min). The retention of amorphous nature with the corresponding change in the vibrational level has been observed from x-ray diffraction (XRD) and Raman analysis. Even after laser irradiation, the homogeneous and smooth texture of the thin film's morphology has been confirmed by the field emission scanning electron microscope (FESEM), and consecutive elemental analysis with mapping has been done by energy dispersive x-ray spectroscopy (EDX) analysis. The reduction nature of transmittance and photodarkening behavior of the optical energy gap was observed from the transmittance data from a UV–Vis–NIR spectrophotometer for the wavelength range of 750–2500 nm. The hydrophilic nature of the irradiated laser films has been confirmed through contact angle measurement, which makes them possible applicants for self-cleaning, antifouling, and antifogging as coating materials.

II. EXPERIMENTAL PROCEDURES

The well-adopted melt-quenching method is used to prepare $Bi_{15}In_{20}Se_{65}$ bulk alloy. A stoichiometric mixture of In, Bi, and Se elements with a purity of 99.999% has been taken in a quartz ampoule which is then vacuum-evaporated. The ampoule was then heated at a slow heating rate (3–4 °C/min) to 500 °C inside the furnace for 20h with constant rocking to achieve a homogeneous mixture of the elements. To avoid crystallinity, the melt is quickly quenched in ice-cold water.

The $Bi_{15}In_{20}Se_{65}$ thin films are prepared from the powdered bulk alloy using a high vacuum coating unit (HINDI-HIVAC Model 12A4D, India) at 10^{-5} Torr. The films are deposited on clean corning glass substrates. The attached thickness monitor maintained the deposition rate (0.5 nm/s) and thickness (800 nm). The constant rotation of the substrate gives homogeneous and smooth films.

The laser irradiation of these films is done by using a 532 nm laser source (~2.33 eV) having a laser intensity of 58 mW cm^{-2} (model—PSU-III-LED, C192055). The incident pump beam was expanded with a beam expander to cover a larger area of the film under investigation. The laser beam is focused on irradiating an area of ~3 mm radius that is mounted on a sample holder. This study includes laser irradiation on thin films with different time variations of 0, 10, 20, 30, 60, and 90 min.

The XRD characterization is done with a Bruker D8 Advance diffractometer through Cu K_α ($\lambda = 1.54$ Å) as the incident ray, operating at 30 kV voltage and 40 mA current over the angular range 10°–80° with a step size of 0.3°/s at and a scan speed 10/min. The Raman study is performed with RENISHAW inVia Raman Microscopy (model—RE 04) by using a 514 nm argon laser with a CCD detector over 50–400 cm^{-1}. FESEM (JEOL, JSM-7601F Plus) is employed for morphological and elemental analyses, which operated at around 20–200 kV voltage during the process. EDX measurement is done to analyze the elemental distribution of these samples with the attached EDX system with FESEM using a 20 kV voltage. The film's optical transmission data have been recorded

using a UV–Vis–NIR spectrophotometer (model—V-760, JASCO) over 750–2500 nm. The contact angle measurement was done using a contact angle meter (model—Dme-211 Plus).

III. RESULTS AND DISCUSSIONS

A. Structural study

XRD analysis is an important characterization that provides a gateway for the study of structural alteration caused by laser irradiation of the sample. Figure 1(a) presents the XRD patterns of laser-irradiated $Bi_{15}In_{20}Se_{65}$ films with different exposure durations. The lack of a sharp peak and the presence of broad humps indicate the non-crystalline nature of the film even after laser irradiation. These humps are the signature of the polymeric nature of material containing selenium and also indicate the short-range ordering inside the matrix.[9,21] The presence of two amorphous humps might be interpreted in terms of the findings of two amorphous phases.

Raman analysis is a chemical method to determine the crystal phase, molecular interactions, and chemical structure. The vibrational level analysis includes the study of structural rearrangements and reformations caused by laser irradiation. The Raman spectra of different time laser-irradiated $Bi_{15}In_{20}Se_{65}$ thin films are presented in Fig. 1(b) which shows various peaks between 50 and 400 cm^{-1}. The spectra comprise four vibrational bands positioned at 68, 95, 127, and 171 cm^{-1}, respectively. The former peak at 68 cm^{-1} corresponds to the A^1_{1g} vibrational phonon mode of the Bi_2Se_3 phase vibrational bond,[22] while the latter peak at 95 cm^{-1} corresponds to the In–Se phase.[23] The prominent peaks at 127 and 171 cm^{-1} are related to E^2_g and A^2_{1g} modes of the Bi_2Se_3 band.[24] Here, the peak shifting and intensity variation might be due to the change in the structural level due to laser irradiation.

B. Morphological analysis

FESEM is one of the most used imaging technique for studying the microstructure and morphology of the material. It is commonly used in the semiconductor industry to produce two-dimensional images by generating contrast features on the material surface by differential charging. The surface morphological structure of all laser-illuminated films with different magnifications is presented in Fig. 2. The lower magnification FESEM images (over scale 1 μm) of 0, 30, and 90 min laser-irradiated thin films clearly show the smoothness and homogeneity nature whereas the increase in magnification (inset images over scale 100 nm) showed smooth texture for 30 and 90 min irradiated films and a slightly cracked texture for the 0 min irradiated film. This crack formation in the 0 min irradiated film might be due to the tensile stress subjected during thermal evaporation. With the increase in the laser irradiation duration, the cracks were annihilated by forming a homogeneous and smooth texture which might enhance the electron transport.[25] There is no evidence of phase transformation observed, which infers that no structural changes occurred, as confirmed by the XRD spectra. The images do not show any growth of the particles, which also ensures the non-crystalline nature of the irradiated thin films.

The EDX analysis of laser-irradiated $Bi_{15}In_{20}Se_{65}$ thin film infers the presence of elements (Bi, In, and Se) in the material [Fig. 3(a)]. The EDX spectra are taken over different regions of the thin film and uniformity and homogeneity over elemental compositions are confirmed. The composition of different elements as obtained for different laser-irradiated films is given in Table I. The composition of laser-irradiated films with different lasing times showed approximately 2% error from the calculated values. Figures 3(b)–3(d) represent the elemental mapping images of the 90 min laser-irradiated Bi–In–Se thin film comprising Bi, In, and Se elements with merged mapping images presented in Fig. 3(e), respectively. The mapping images clearly demonstrate the uniform distribution of the respective elements throughout the sample. For better clarity over elemental distribution, EDX and elemental mapping are carried out at a particular thin film region.

C. Optical analysis

1. Linear optical parameters

a. Transmission (T), reflectance (R), and absorption coefficient (α). The optical property study of thin films emphasizes the

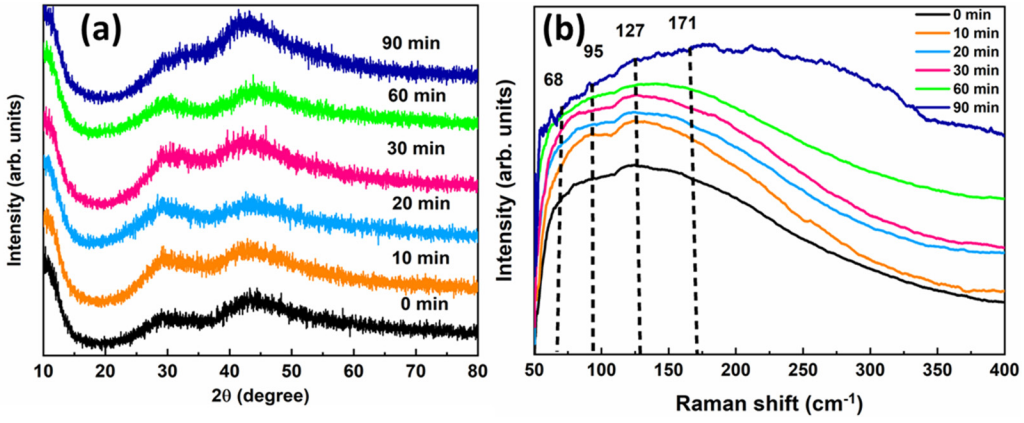

FIG. 1. (a) XRD pattern and (b) Raman spectra of different time-varied laser-irradiated $Bi_{15}In_{20}Se_{65}$ thin films.

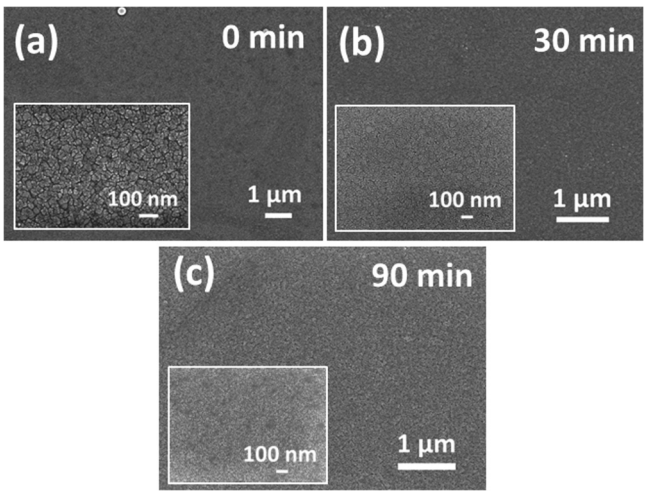

FIG. 2. FESEM micrographs of (a) 0, (b) 30, and (c) 90 min laser-irradiated $Bi_{15}In_{20}Se_{65}$ thin films for different magnifications (inset scale: 100 nm).

optimal use of related materials in all modern applications. Transmission and absorption are the primary focal points for understanding the material's optical behavior. The transmittance and reflectance spectra of different time-varied laser-irradiated $Bi_{15}In_{20}Se_{65}$ films over 750–2500 nm wavelength is shown in Fig. 4(a). In the transmittance and reflectance spectra, the appearance of interference fringes depicts the homogeneous and uniform nature of irradiated films. The spectral behavior of transmittance for the studied laser-irradiated films is split into three major regimes: (a) strong absorption (>900 nm), (b) absorption edge (900–1200 nm), and (c) weak absorption [>1200 nm, over near-infrared (NIR) regime]. Weak absorption is attributed to the localized states formed by defects and disorders in the semiconductor material.[26] Irradiated film transmittance is primarily enhanced and then reduced for the lasing duration, which could be attributed to the change in the lattice defects and localized states across the bandgap regime.[27] The overall maximum transmission reduced from 80% (0 min) to 67% for the 90 min laser-irradiated film, particularly in the NIR region. In the NIR regime, n, the interaction between free electrons and incident radiation is more due to the thin film's large number of free electrons. This interaction might result in the polarization of light in the films, by causing a prominent change in the transmission spectra. This behavior ultimately affects the dielectric response of the material. Thus, the overall reduction with lasing duration might be due to the free carrier absorption, which is typically useful for high-carrier concentration-based transparent conductors.[28] However, the broad transparency over the IR region makes these films appealing for fabricating optical devices such as lenses, fibers, or planar waveguides. Particularly, the large transparency and less absorption in the far- and mid-IR regions of these materials could also be potential in IR optics such as temperature detection, energy management, monitoring, night vision, etc.[29,30]

The red shifting of the optical absorption edge to a higher wavelength with lasing duration is observed from the inset of

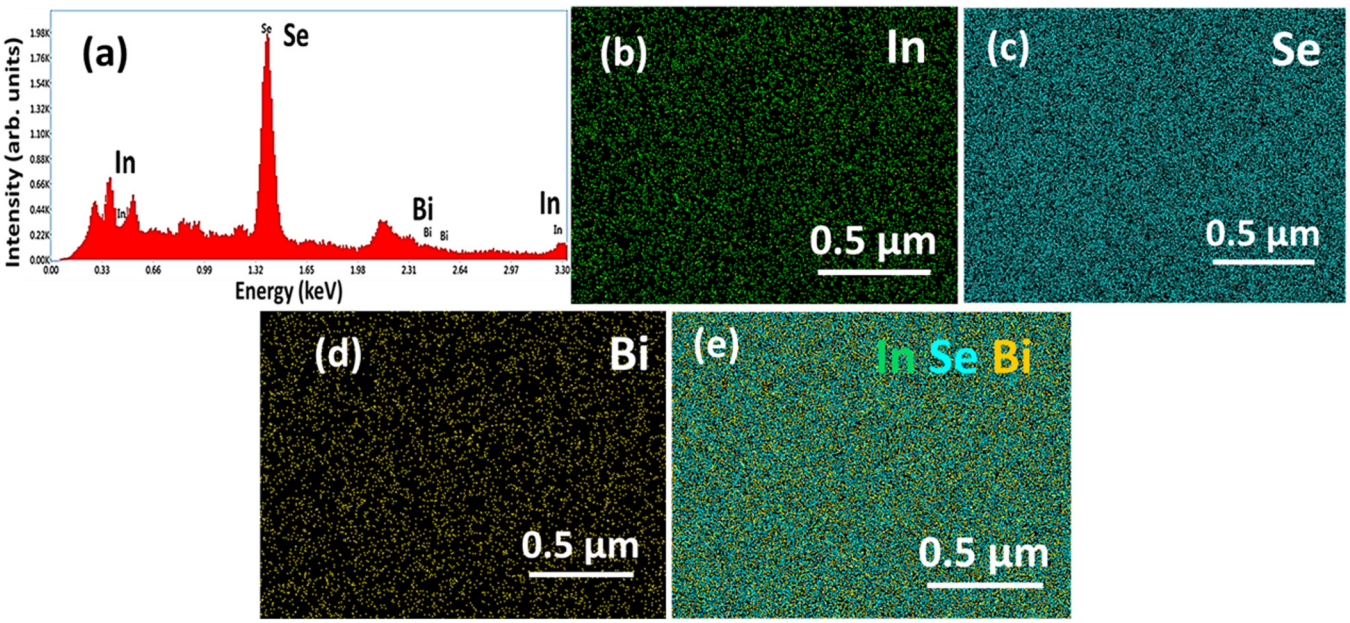

FIG. 3. (a) EDX spectrum, (b)–(d) corresponding individual elemental mapping of Bi, In, and Se, and (e) the mixed mapping of all elements of 90 min laser-irradiated $Bi_{15}In_{20}Se_{65}$ thin films.

TABLE I. EDX compositional data for all laser-irradiated $Bi_{15}In_{20}Se_{65}$ thin films.

Sample	0 min		10 min	20 min	30 min	60 min	90 min
Element	Cal (at. %)	Obs (at. %)	Obs (at. %)	Obs (at. %)	Obs (at. %)	Obs (at. %)	Obs (at. %)
Bi	15	14.10	14.35	14.64	14.07	14.60	14.29
In	20	19.79	20.39	21.01	20.59	20.68	19.70
Se	65	66.11	65.26	64.35	65.34	64.72	66.01
Total	100	100	100	100	100	100	100

Fig. 4(a). This indicates the red shifting with lasing time, which signifies the reducing nature of E_g. When the incident radiation energy reaches the forbidden energy value, the absorption value of the material is sharply increased, indicating the optical absorption edge, and the corresponding wavelength at the optical absorption edge known as the cut-off wavelength.[31] Here, the absorption edge appears between 900 and 1200 nm with a more sharp nature and moves toward the higher wavelength as the lasing duration increases by defining the photodarkening nature. Similarly, the absorption behavior of these samples can be measured by the absorption coefficient (α). This is mainly used in determining many optical parameters in amorphous films, which define as the ratio of absorbed radiant energy incident on the semiconductor material with the material distance toward the propagation direction.[31,32] It is also related to the electronic transition occurring between VB and CB, which is determined from the transmittance (T) using the following relationship:[33]

$$\alpha = \left(\frac{1}{t}\right)\ln\left(\frac{1}{T}\right). \quad (1)$$

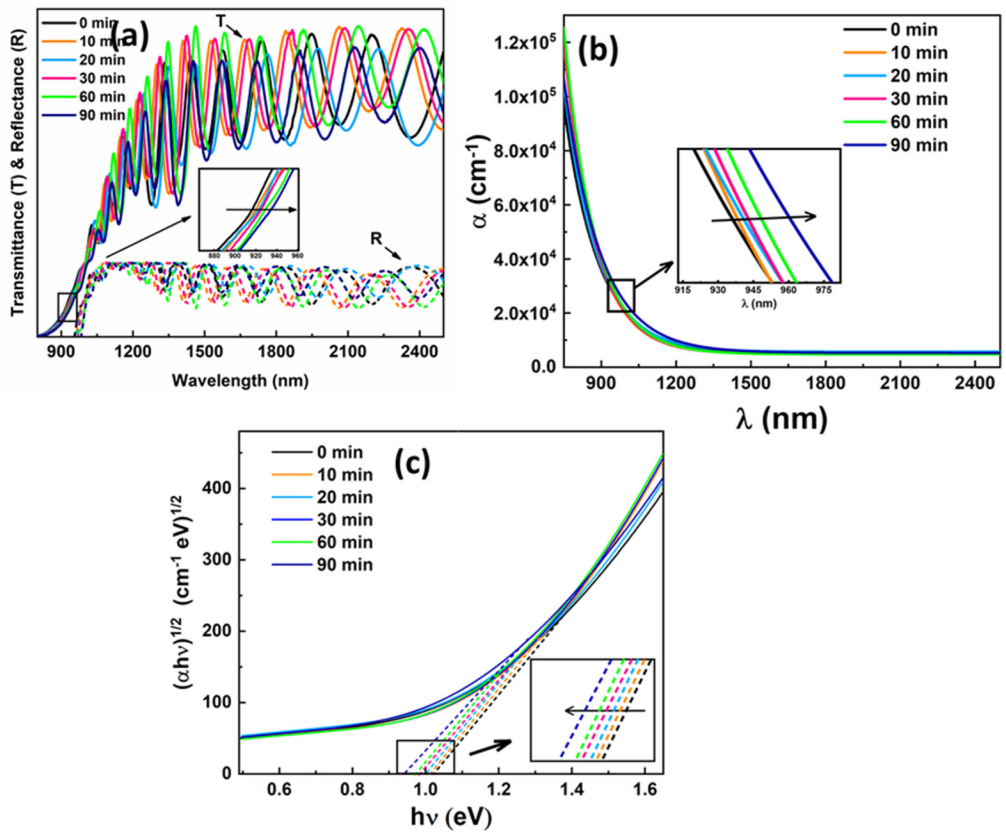

FIG. 4. (a) Optical transmittance and reflectance spectra, (b) absorption coefficient spectra showed the increase in absorption capability with red shifting of absorption edge, and (c) variation of Tauc's optical energy gap (E_g) values for different time-varied laser-irradiated $Bi_{15}In_{20}Se_{65}$ films.

TABLE II. The estimated E_g, $B^{1/2}$, E_u, and σ of different laser-irradiated $Bi_{15}In_{20}Se_{65}$ thin films.

Samples	0 min	10 min	20 min	30 min	60 min	90 min
E_g (eV)	1.024	1.010	1.002	0.980	0.971	0.945
$B^{1/2}$ ($cm^{-1/2}$ $eV^{1/2}$)	640	620	613	607	604	560
E_u (eV)	0.228	0.230	0.232	0.247	0.249	0.250
Σ	0.112	0.110	0.109	0.104	0.103	0.102
E_{e-p}	13.39	13.64	13.77	14.42	14.56	14.71

Here, "t" refers to the film thickness (800 nm). The change in "α" for different irradiated samples is presented in Fig. 4(b). The "α" value is $\sim 10^4\,cm^{-1}$ over the visible and near the absorption edge (NIR region). With increasing wavelength, "α" values dropped after the absorption edge and showed saturation with a very low value. This denotes more transparent behavior with a higher wavelength region. The increase in lasing duration increased the absorption coefficient and shifted to a higher wavelength IR region, as seen from the inset Fig. 4(b).

b. Urbach energy (E_u) and band energy (E_g). In chalcogenide materials, a typical absorption edge has been typically classified into three regions such as weak absorption region, Urbach region, and Tauc region. The defects near the optical band edge led to Urbach tails, and the corresponding thicknesses sometimes extend beyond E_g.[34] So, the Urbach tail is presented by the absorption edge region over $\alpha < 10^4\,cm^{-1}$, allowing photon absorption among the localized tail states and extended band states. According to the Urbach formula, the exponential behavior of "α" with "hν" represents the absorption mechanism over the weakly absorbing regime,[35]

$$\alpha = \alpha_0 e^{\frac{h\nu}{E_u}} \Rightarrow \ln\alpha = \ln\alpha_0 + \frac{h\nu}{E_u}, \tag{2}$$

where "α_o" is a constant that depends on E_g, T, and film thickness, ν is the incident radiation frequency, h is the Planck's constant, and E_u is the Urbach energy, which signifies the width of the band tail of the localized states in the bandgap. The relation between ln(α) and $h\nu$ yields a straight line, and "E_u" is estimated from the inverse slope of the graph's linear part, tabulated in Table II. The "E_u" values enhance with the lasing duration, which signifies an increment in disorders and defects inside the material due to laser irradiation. These defects and disorders enhance the localized states over the band region by reducing the optical energy gap between the valence and conduction bands.[28] The disorder could be from intrinsic defects caused by point defects like vacancies, interstitials, or dislocations due to laser irradiation and external factors might be due to deviation from stoichiomentry.[36]

In amorphous semiconductors, according to Urbach, the band-tail width energy and "α" can be presented as[37]

$$\alpha = \mu \exp\frac{\sigma(h\nu - E_u)}{KT}, \text{ in other way } \ln\alpha = \ln\mu + \frac{\sigma(h\nu - E_u)}{KT}, \tag{3}$$

where μ is the pre-exponential factor, σ is the steepness parameter that presents the broadening of edge, K is the Boltzmann constant, and T is the absolute temperature. As per the electronic transition energy, $E_o = E_g + E_p$, where $E_o = E_g$ represents the allowed direct electronic transition. Thus, on comparing and rearranging the steepness parameter (σ) given by[36] $\sigma = \frac{KT}{E_u}$. The steepness parameter mainly contributes toward the electron–phonon interactions, reflecting the disorder related to the structural and compositional behavior in the samples. The estimated "σ" tabulated in Table II shows the reduction pattern. The localized states at the lower energy regions increase "E_u" and decrease "σ."[36,37] This reduction indicated enhancement in the electron–phonon interaction, which is presented by $E_{e-p} = 3/2\sigma$.[37] The estimated E_{e-p} values are presented in Table II. It is found that the value of "E_{e-p}" enhanced with the irradiation duration that inversely varies with "σ."

The Urbach and Tauc regions have values of $\alpha < 10^4$ and $\alpha > 10^4\,cm^{-1}$, respectively. The Urbach plot is determined by the linear fit to the transition between defects caused by the localized states; thus, sub-gap absorption occurs at photon energies less than the sample's E_g, whereas the Tauc plot is determined by the linear fit to the main absorption edge.[30] Thus, a region corresponding to the high absorption value where $\alpha \geq 10^4\,cm^{-1}$ is known as the Tauc regime, which is used for the determination of the E_g of the material. According to Tauc's relation,[38,39]

$$(\alpha h\nu) = B(h\nu - E_g)^p, \tag{4}$$

where ν is the incident beam frequency. The Tauc parameter is presented by $B^{1/p}$, which depicts the degree of disorder over the bandgap regime, and "p" presents the type of transition (direct or indirect) and the electron-density profile over the valence and conduction bands. It characterizes the transition process, p is 1/2 for the direct allowed transition, 3/2 for direct forbidden, 3 for indirect forbidden, and 2 for the indirect allowed transition. In crystalline materials, the fundamental absorption edge is due to the direct electron transition between the valence and conduction bands (direct allowed transition, $p = 1/2$). In contrast, in amorphous

materials, the transition is referred to as non-direct (indirect allowed transition, $p = 2$) due to the lack of an electronic band structure in k-space. Here, different irradiated films showed amorphous nature confirmed by XRD analysis. Thus, optical transition in the studied films is due to the indirect allowed transition. The linear fitting of $(\alpha h\nu)^{1/2}$ with the "$h\nu$" plot gives "E_g" from the horizontal intercept along the energy axis, and the slope provides the Tauc parameter. The estimated "E_g" values for different laser-irradiated films are noted in Table II. The value of "E_g" reduces as the exposure duration enhances [the inset in Fig. 4(c)], which signifies PD behavior. This behavior might be due to the new level addition near to the valence band as a consequence of the increase in the exposure period, which leads to the creation of bridges to cross electrons transmitted from the valence band to the conduction band. These bridges, also called localized states, have lower energies than the "E_g" value of the corresponding materials.[32] In another way, according to the "density of state model" proposed by Mott and Davis, the mobility edge is affected by the defects and disorders in the film.[40,41] The application of external energy inputs (in this case, laser irradiation) to the material induces modification inside the material structure through bond breaking, bond angle variations, and bond rearrangement, resulting in a change in local structure in the amorphous network. These atomic rearrangements produce defects and disorders such as dangling bonds and unsaturated bonds with energy lower than the forbidden gap energy. This increases the density of localized states while decreasing "E_g" and increasing the probability of transitioning from the band-tail states. Such behavior has been observed in other studies as well.[40–43] The Tauc parameter ($B^{1/2}$) represents the tailing parameter and inverse nature with the degree of the disorder. Here, "$B^{1/2}$" shows a reduced pattern in Table II, which depicts the increase in disorders inside the system with exposure duration.

c. Skin depth and optical density. Skin depth (δ) explains the penetration of electromagnetic waves inside the thin film where the incident radiation reduces exponentially. It is derived from the reciprocal of "α," i.e., $\delta = 1/\alpha$. Figure 5(a) depicts the variation of "δ" with $h\nu$. With an increase in energy, "δ" decreases and becomes zero after the cut-off energy of 1.3 eV. This value varies slightly with the lasing time.

The optical density (OD) presents the material's absorption ability when exposed to electromagnetic radiation and is calculated

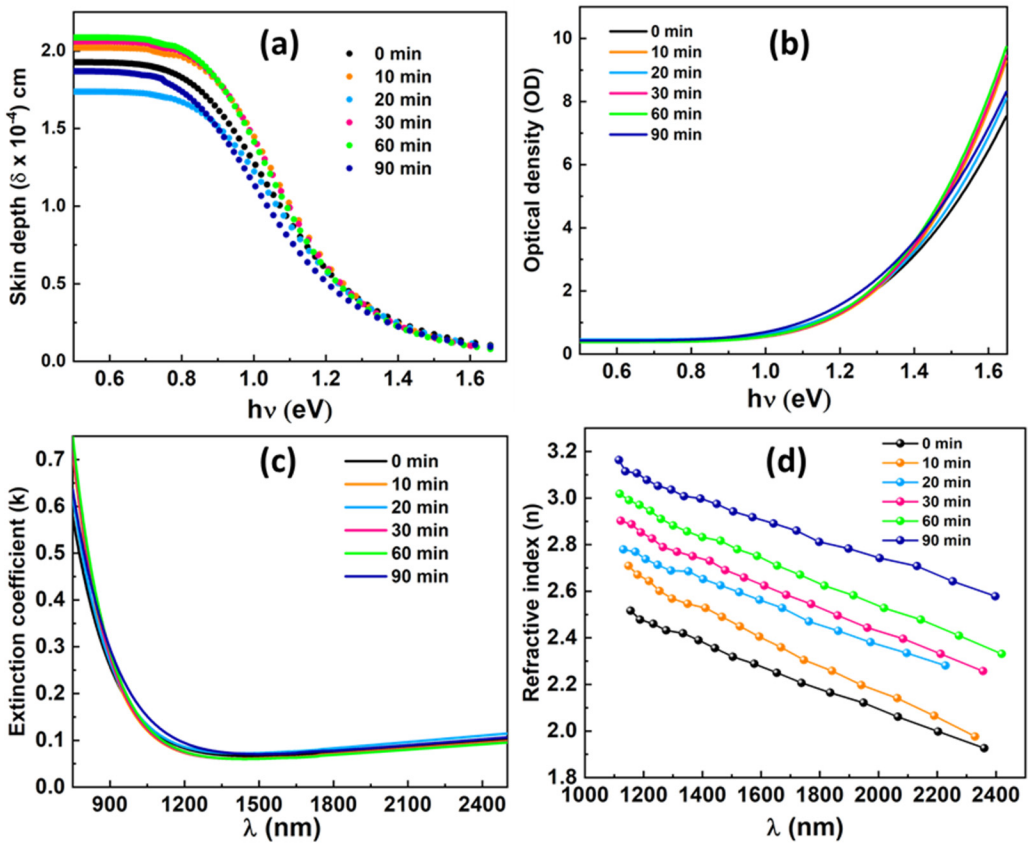

FIG. 5. (a) Dependent of skin depth and (b) OD upon the hν, increase in (c) extinction coefficient and (d) refractive index upon wavelength for different laser-irradiated $Bi_{15}In_{20}Se_{65}$ films.

by using[44] "α" and "t," OD = OD = α × t, where "t" represents the film thickness (800 nm). Figure 5(b) illustrates the "OD" variation with energy which shows a small variation in the "OD" value with exposure time and saturation at the lower energy region.

d. Refractive index (n) and extinction coefficient (k). The complex refractive index $\tilde{n} = n + ik$ provides information on the transmitted electromagnetic wave velocity through the medium. The real part of $\tilde{n}$ (n) is related to light beam velocity, and the imaginary part is related to the deterioration of vibrational frequencies of the incident electric field. The interaction between the medium and the electric field primarily supports the optical properties of the material.[45] The "k" value is calculated by using "α" and "λ" as[45,46] $k = \frac{\alpha\lambda}{4\pi}$. The variation of k with λ is shown in Fig. 5(c), which shows a slight increase with different laser exposure durations and saturates at higher wavelength NIR regimes. Over the NIR region, "α" is low, and the transmittance is high, so the dissipation coefficient, "k" is the lowest. Thus, "α" and transmittance are primarily responsible for this behavior.[45] Furthermore, "k" also describes how much energy a light beam loses due to absorption in the medium through which it passes.[47] Tuning of the "k" value causes a change in the non-linear behavior of the material. Furthermore, "k" values approach zero at higher wavelengths, implying that incident electromagnetic waves easily pass through the material with negligible loss and decay. Such behavior indicates that there is no scattering or loss of energy of the incident electromagnetic waves in the IR and NIR regions, making them ideal for IR and NIR optical applications.[48]

The Swanepoel envelope method is employed for refractive index (n) estimation for these laser-irradiated films.[2] According to this envelope method, the first approximated refractive index "n_1" is calculated for the region of weak and moderate absorption by

$$n = \left[N + (N^2 - s^2)^{\frac{1}{2}} \right]^{1/2}, \tag{5}$$

where $N = 2s\left[\frac{T_M - T_m}{T_m T_M}\right] + \frac{s^2+1}{2}$, "$T_m$" and "$T_M$" are the minimum and maximum of the transmittance curve at a given wavelength, and "s" is the substrate refractive index (1.51). Following the procedure detailed in the literature,[49] the estimated "n" variation is presented in Fig. 5(d). The "n" decreases as the wavelength increases, indicating that thin films have normal dispersion behavior. With increasing laser exposure time, the "n" increased significantly. Such materials with high "n" values have great relevance for improving the optical intensity of the material. The observed "n" values range between 2.2 and 3.1, which could be utilized for designing integrated circuits, ultrafast optical devices, IR sensors, and so on.[50] The opposite trend of "E_g" with "n" value follows the Moss relation $E_g n^4 \sim$ constant.[51] The change in "k" and "n" values with the lasing duration affects the electronic polarizability and non-linear properties of the material. Moreover, both "k" and "n" reduced as the wavelength increased and enhanced with the lasing duration. This indicates the reduction of transmittance and an increment in the scattering centers.[45]

e. Dielectric constants and loss factors. Studying the behavior of "k" in association with "n" in semiconductors provides a good understanding of dielectric constants and loss factors.[26] Thus, the real and imaginary parts of the dielectric constants of laser-irradiated films with different lasing durations were estimated by using the following equations:[46]

$$\varepsilon_1 = n^2 - k^2 \text{ and } \varepsilon_2 = 2nk. \tag{6}$$

Here, "ε_1" and "ε_2" represent the real and imaginary parts of complex dielectric constants, which are responsible for electromagnetic wave dispersion inside the semiconducting material and energy absorption due to electric dipolar motion. The real part depicted the slowing of photons as they propagated, while the imaginary part measured the rate of photon disturbance.[26] Figures 6(a) and 6(b) depict the spectral distribution of "ε_1" and "ε_2" for different laser-irradiated films with wavelength. The figures clearly show that "ε_1" is many times (ten times) greater than "ε_2." This observation is due to $n \gg k$ for the "ε_1" case, while for the "ε_2" case, the low "k" value reduced the imaginary part to below 0.8. Both "ε_1" and "ε_2" enhanced with the lasing duration, which infers the enhancement in the energy dispersion rate of incident radiation, which led to the reduction in the propagation velocity of the electromagnetic wave incident on the material.[26] The observed variation of these dielectric parameters showed a good optical response for laser-irradiated $Bi_{15}In_{20}Se_{65}$ thin films. The dissipation factor of the dielectric loss provides information on the difference in phase caused by energy loss within the material at a particular frequency, which is presented as, $\tan\delta = \varepsilon_2/\varepsilon_1$. Figure 6(c) presents the spectra of the dielectric loss of all-irradiated films, which show a reducing trend with lasing duration. At shorter wavelengths, "tan δ" is relatively higher, while it reduces at a wavelength of ∼1200 nm and then enhances with the NIR wavelength region.

f. Dispersion parameters and carrier concentration. The dispersion behavior of "n" is investigated using the Wemple–DiDomenico model, which depicts the change of "n" with incident photon energy. The "n" is related to hν, E_o, and E_d via the following relation:[52]

$$(n^2 - 1) = \frac{E_0 E_d}{E_0^2 - (h\nu)^2} \Rightarrow (n^2 - 1)^{-1} = \frac{E_o^2 - (h\nu)^2}{E_o E_d} = \frac{E_o}{E_d} - \frac{(h\nu)^2}{E_o E_d}. \tag{7}$$

Figure 7(a) shows $(n^2-1)^{-1}$ vs $(h\nu)^2$ variation for all laser-irradiated films. The slope $(1/E_oE_d)$ and intercept (E_o/E_d) of the straight-line fitting are used to calculate the E_o and E_d values. The dispersion energy (E_d) measures the average interband strength of an optical transition and is related to various parameters such as effective valency electrons per anion and coordination number. However, the WDD gap, also known as oscillator energy "E_o," defines the distance between the center of gravity of the material's CB and VB and, thus, correlates with bond strength. This model relates three types of energies, such as (i) the effective oscillator energy E_o (average energy gap), (ii) dispersion energy (E_d), and (iii) incident photon energy. This model mainly relies on the refractive index of a semiconducting material and its dispersion behavior

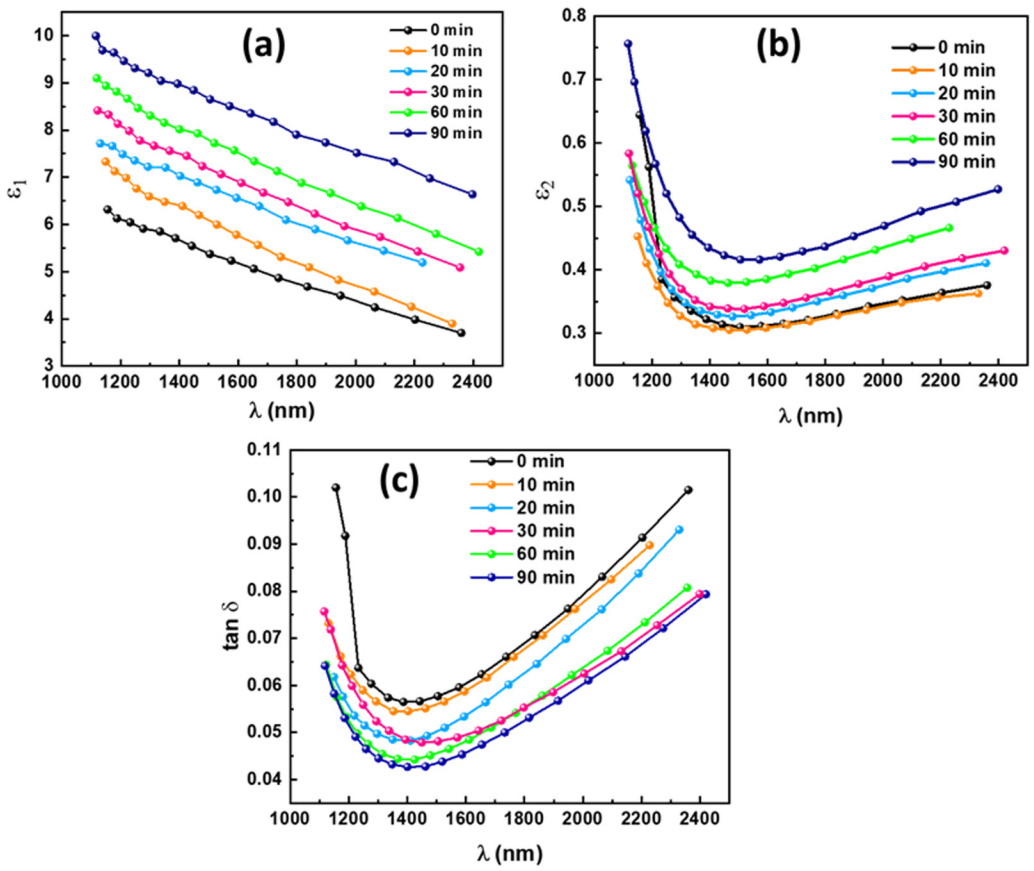

FIG. 6. The spectra of (a) real part (ε_1) and (b) imaginary part (ε_2) of the complex dielectric constant and (c) the tangential loss (tan δ) of all laser-irradiated films with different lasing durations.

below the interband absorption edge with wavelength and energy. Additionally, with reasonable extinction coefficient values, several studies on the dispersion behavior of semiconducting materials have been done by using the WDD model.[38,47,53] Table III summarizes the estimated dispersion energy values, which showed the value of "E_o" reduced with the exposure time, while "E_d" showed an increment with the same. The reduction in "E_o" explains that the system becomes more relaxed, stable, and rigid with laser irradiation.[53] The obtained values of "E_o" behave hormonally with band energy, i.e., approximately satisfy the empirical relation[54] $E_o \approx 2E_g$. The obtained E_o/E_g ratio for different irradiated films is tabulated in Table III. Here, the ratio varies from 1.6 to 1.85, which has been observed in other studies.[31,38,55]

Furthermore, "E_d" measures the interband transition intensity. Thus, with the increase in exposure time, the interband transitions inside the system enhance. Moreover, an increase in E_d due to an increase in the lasing duration causes more disturbances or disorder in the bandgap region, thereby enhances the localized state density and, in turn, reduces "E_g."[56] Other than that, it also related with the other physical parameters of materials, which is expressed as $E_d = \beta N_c N_e Z_a$, where the constant "β" has two values such as $\beta_{ionic} = 0.26 \pm 0.03$ eV and $\beta_{covalent} = 0.37 \pm 0.04$ eV, "N_c" is the effective coordination number of the cation nearest-neighbor to the anion, "N_e" is the effective coordination number of valence electrons per anion, and "Z_a" is the chemical valence of the anion.[57] Therefore, the "E_d" enhancement with exposure time might be due to the enhancement in the values of "N_c" and "N_e."

The transition moments of the optical spectra, "M_{-1}" and "M_{-3}," evaluated from the obtained "E_o" and "E_d," values by using the WDD model are given as[58]

$$E_o^2 = \frac{M_{-1}}{M_{-3}} \text{ and } E_d^2 = \frac{M_{-1}^3}{M_{-3}}.$$

Rearranging the above equations as follows:

$$M_{-1} = \frac{E_d}{E_o} \text{ and } M_{-3} = \frac{M_{-1}}{E_o^2}. \quad (8)$$

Table III shows the estimated "M_{-1}" and "M_{-3}" enhancement with laser duration. Both "M_{-1}" and "M_{-3}" rely on "E_o" and "E_d," since $E_d > E_o$, M_{-1} and M_{-3} follow the same trend as "E_d." The

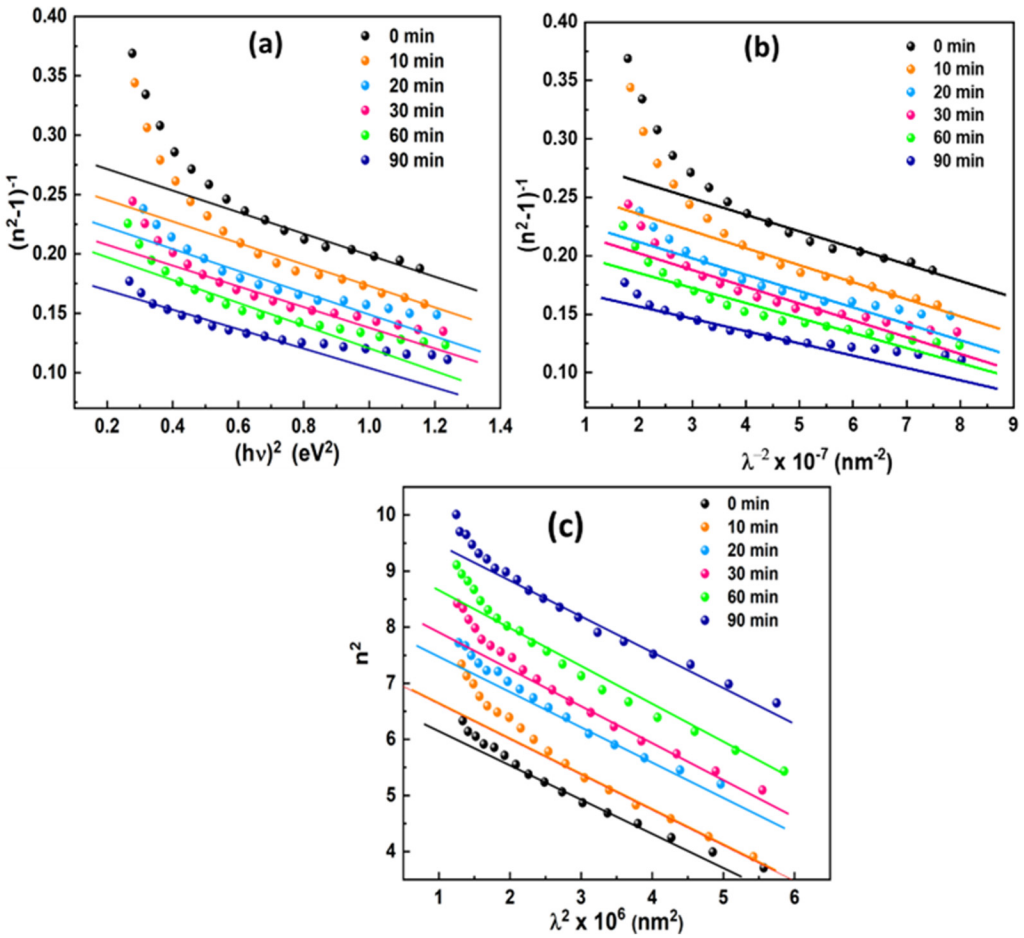

FIG. 7. Refractive index dispersion via (a) WDD model in $(n^2-1)^{-1}$ vs $(h\nu)^2$ plot and (b) Sellemeier model in $(n^2-1)^{-1}$ vs $(\lambda)^{-2}$ plot, and (c) determination of high-frequency dielectric constant (ε_L) and carrier concentration (N/m*) from n^2 vs λ^2 plot for different laser-irradiated $Bi_{15}In_{20}Se_{65}$ films.

oscillator strength of the films can be denoted as $f = E_o E_d$. The oscillator strength values showed an increment with exposer duration. Furthermore, the zero-frequency dielectric constant of the lattice (ε_L) and static refractive index (n_o) (where $h\nu \to 0$) has been calculated using the following relationship:[59]

$$\varepsilon_L = 1 + \frac{E_d}{E_0} \text{ and } n_o = \sqrt{1 + \frac{E_d}{E_o}},\ \varepsilon_L = (n_o)^2. \tag{9}$$

The calculated "ε_L" and "n_o" increased with an increase in the exposure duration as seen in Table III. The variation of "ε_L" and "n_o" satisfies the trend observed in the refractive index plot [Fig. 5(d)].

Sellmeier deduced that the "n" at a high wavelength (low hν) follows the classical dispersion relation and thus obtained the relations for oscillator strength "S_o" and wavelength "λ_o" as follows:[56]

$$\frac{n_0^2 - 1}{n^2 - 1} = 1 - \frac{\lambda_0^2}{\lambda^2}, \tag{10}$$

where "λ_o" represents the oscillator wavelength. The variation of $(n^2-1)^{-1}$ with λ^{-2} is shown in Fig. 7(b). For $S_o = (n_o^2-1)/\lambda_o^2$, where "$S_o$" denotes the average oscillator strength, the above Eq. (8) becomes

$$\frac{1}{n^2 - 1} = \frac{1}{\lambda_o^2 S_o} - \frac{1}{S_o \lambda^2}. \tag{11}$$

Using the slope and intercept of the graph, "S_o" and "λ_o" are obtained and presented in Table III. It is observed that both "S_o" and "λ_o" values increased with the lasing duration. "λ_o" is inversely dependent on "E_o" and "S_o" is related to "E_d;" therefore, $\lambda_o \propto 1/E_g$.

TABLE III. The estimated optical parameters of different laser-irradiated $Bi_{15}In_{20}Se_{65}$ thin films.

Optical parameters	0 min	10 min	20 min	30 min	60 min	90 min
Single oscillator energy (E_o) eV	1.77	1.69	1.61	1.57	1.58	1.74
Dispersion energy (E_d) eV	6.08	6.45	6.58	6.72	7.49	10.11
E_0/E_g	1.73	1.68	1.61	1.61	1.63	1.85
Static linear refractive index (n_o)	2.10	2.19	2.25	2.30	2.39	2.61
The lattice dielectric constant (ε_L)	4.42	4.81	5.08	5.29	5.73	6.81
The first moment (M_{-1})	3.42	3.81	4.08	4.29	4.73	5.81
The second moment (M_{-3})	1.08	1.32	1.57	1.75	1.89	1.92
Oscillator strength (f)	10.80	10.93	10.60	10.53	11.85	17.57
Oscillator wavelength, λo (nm)	699.59	733.32	771.27	793.12	804.60	815.58
Oscillator strength (S_o) $nm^2 \times 10^{-6}$	7.00	7.08	6.87	6.83	7.68	11.38
High-frequency dielectric constant (ε_L)	6.88	7.25	8.45	9.06	9.69	10.58
Carrier concentration ($N/m^* \times 10^{38}$) $(Kg\,m^3)^{-1}$	7.52	7.73	8.60	9.46	9.63	9.67
Linear susceptibility ($\chi^{(1)}$)	0.27	0.30	0.32	0.34	0.37	0.46
Third-order non-linear susceptibility ($\chi^{(3)} \times 10^{-12}$ esu)	0.94	1.44	1.91	2.32	3.44	7.80
Non-linear refractive index ($n_2 \times 10^{-11}$ esu)	1.68	2.47	3.19	3.81	5.41	11.26
Optical electronegativity (η_{Opt})	1.87	1.85	1.83	1.82	1.81	1.77
Plasma frequency ($\omega_p^2 \times 10^{10}$) Hz	7.89	7.70	7.36	7.55	7.18	6.60

Thus, the increment in "λ_o" is attributed to the decrement in "E_g."[27]

The high-frequency dielectric constant (ε_L) and the ratio of carrier concentration per effective mass (N/m^*) are calculated by the given formula:[49]

$$n^2 = \varepsilon_1 = \varepsilon_\infty - \left(\frac{e^2}{4\pi^2 c^2{}_0}\right)\left(\frac{N}{m^*}\right)\lambda^2, \tag{12}$$

where the electronic charge is presented by "e," the number of free charge carriers is "N," the free space permittivity is "ε_o," the free charge carrier effective mass is "m,*" and the velocity of light is "c." Here, the linear extrapolation of the n^2 vs λ^2 plot is shown in Fig. 7(c), which provides the slope value as "N/m^*" and an intercept as "ε_L" which are tabulated in Table III. The carrier concentration per unit effective mass was significantly enhanced with the exposure time.

According to Drude's model, the plasma frequency (ω_p) is a fundamental optical parameter that is given by[60] $\omega_p^2 = \left(\frac{e^2}{4\varepsilon_o\varepsilon_\infty}\right)\frac{N}{m^*}$. The obtained "$\omega_p$" value for these films is tabulated in Table III. The reduction in "ω_p" values with increasing exposure time depicts the modification in the polarization process within the system.[61] "ω_p" also presents the free electron's resonance frequency in their mean position.

2. Non-linear optical parameters

a. Non-linear susceptibility and refractive index. The non-linear phenomenon mainly emphasizes achieving ultrafast optical switching devices and has played an important role in modem optical communication systems with high bit rate signal transmission. This behavior comes into action when the change in the material's polarization response is non-linear to electromagnetic radiation passing through it. However, material polarizability is related to the dielectric parameter, which is determined by the "n" and "k" of the system. The material's "n" is linked to its non-linear property; thus, corresponding changes in the host matrix due to the application of external energy inputs result in subsequent alteration in the material's susceptibility. Therefore, materials with high non-linearity have a lot of potential in soliton propagation in optical telecommunications, parametric amplification, Raman amplification, optical processing, and supercontinuum generation.[62,63] Moreover, when exposed to a highly intense electric field, the material no longer polarizes linearly with the applied electric field, but instead, becomes proportional to the electric field's multipower. Thus, induced polarization (P) is described as a series expansion of applied electric field (E) and susceptibility (χ) of dielectrics as follows:[63]

$$P = \varepsilon_0[\chi^{(1)}.E + \chi^{(2)}.E^2 + \chi^{(3)}.E^3 + \cdots], \tag{13}$$

where "$\chi^{(1)}$" represents the linear part of polarization and "$\chi^{(2)}$" and "$\chi^{(3)}$" represent the second-order and third-order non-linear susceptibilities, respectively. Second-order non-linear susceptibility vanishes in centrosymmetric media while possessing a non-zero value in the systems lacking inversion symmetry. Thus, the majority of non-linear effects in amorphous semiconductors, such as four-wave mixing, third harmonic generation, and non-linear refraction, are contributed from one single non-zero term, third-order non-linear susceptibility ($\chi^{(3)}$).[51] According to Miller's rule, the linear and non-linear optical susceptibility ($\chi^{(1)}$) and ($\chi^{(3)}$) can be estimated as follows:[64,65]

$$\chi^{(1)} = \frac{n_o^2 - 1`}{4\pi} \text{ and } \chi^{(3)} = A(\chi^{(1)})^4 = A\left(\frac{n_o^2 - 1`}{4\pi}\right)^4 = A\left[\frac{E_o E_d}{4\pi(E_o^2 - (h\nu)^2)}\right]^4, \tag{14}$$

where "n_o" is the static refractive index for $h\nu \to 0$ and "A" is a constant with a value of $\sim 1.7 \times 10^{-10}$ (for $\chi^{(3)}$ measured in esu). Table II displays the calculated "$\chi^{(1)}$" and "$\chi^{(3)}$" values which showed improvement in both "$\chi^{(1)}$" and "$\chi^{(3)}$" as the laser exposure duration increased. This could be due to the laser-induced local structural change that increases carrier concentration. Figure 8(a) depicts the observed "$\chi^{(3)}$" with "E_g" variation, which clearly showed the opposite pattern in "E_g" with "$\chi^{(3)}$" with different exposure durations. "$\chi^{(3)}$" at different wavelength regions show the same trend as the refractive index, as shown in the inset Fig. 8(b).

Additionally, the change in the refractive index (Δn) arises due to the non-linear response of the material, presented by, $\Delta n = n_2 |E|^2$, where "n_2" and "E" are presented as the non-linear refractive index and applied electric field, respectively.[66] The non-linear refractive index of the investigated films has been evaluated by using Ticha and Tichy and Miller's rule given by[66,67] $n_2 = \frac{12\pi\chi^{(3)}}{n_o}$. The estimated value of the non-linear refractive index in esu for different laser-irradiated films is shown in Table III. Figure 8(b) presents the "n_2" pattern with wavelength for different exposure time. It increases with the exposure duration, which might be due to the production of defect states by laser irradiation that enhances local polarizabilities.[68]

b. Non-linear absorption coefficient (β) and figure of merit (FOM). Chalcogenide semiconducting materials are well recognized for their two-photon absorption properties. The incident light interaction with chalcogenide semiconductors with high optical non-linearity results in a multiphoton absorption process, making these materials suitable for various photonics devices such as

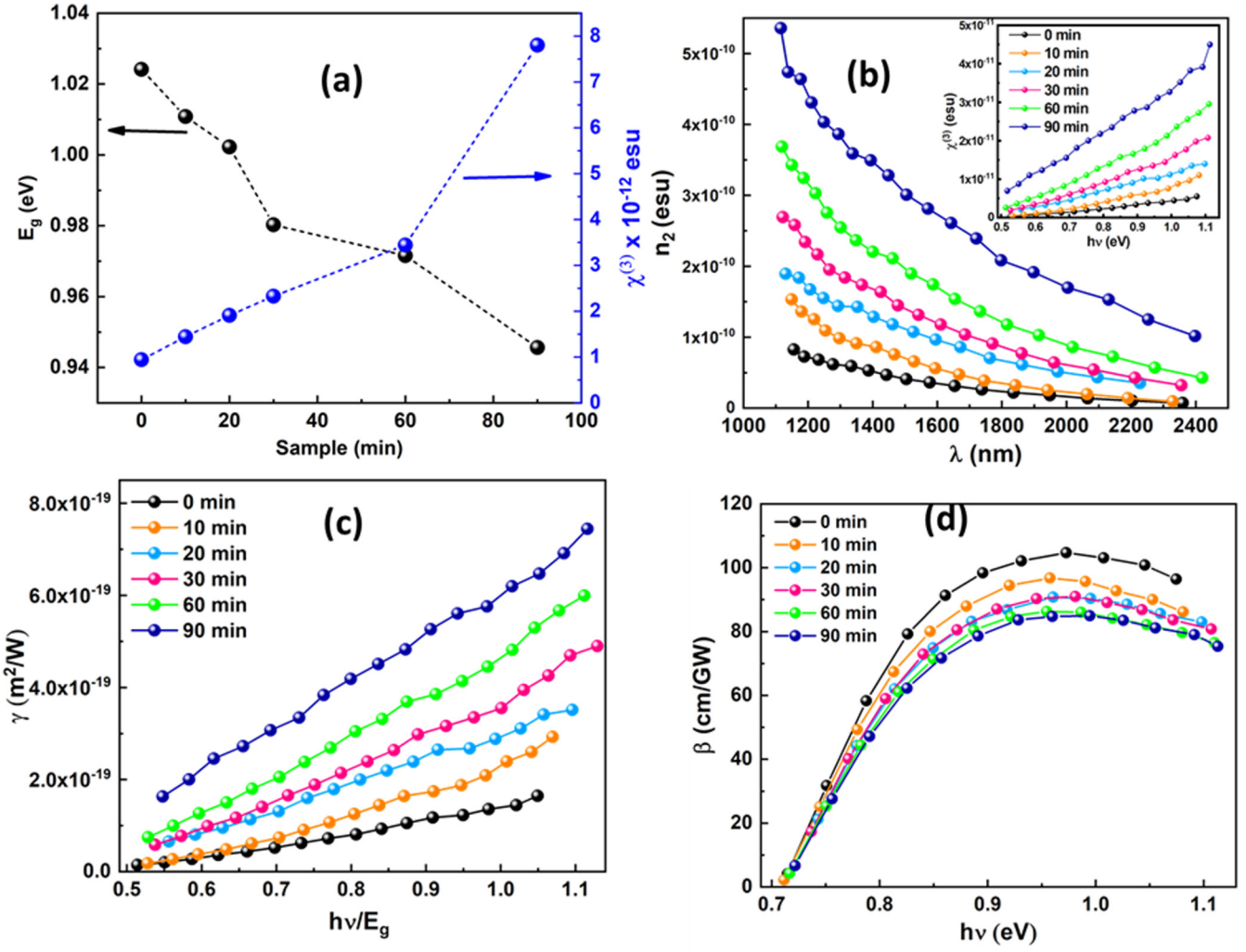

FIG. 8. (a) Variation of non-linear susceptibility ($\chi^{(3)}$) and E_g with exposure time, (b) the change in non-linear refractive index (n_2) and $\chi^{(3)}$ with wavelength and energy, and (c) dispersion of non-linear refractive index in SI, γ and (d) non-linear absorption coefficient β_c for these films.

optical switches, correlators, quantum detectors, and so on. This two-photon absorption (TPA) is primarily a third-order non-linear process in which two or a pair of photons are absorbed while electrons are simultaneously excited from the ground to higher energy states.[69] In the context of maximizing the non-linear index of refraction, minimization in "E_g" always favors. The chalcogenide material medium's non-linear response to intense light with photon energies, $E_g/2 \leq h\nu \leq E_g$ revealed two-photon absorption involving interband transitions. This includes the related term, n_2, as well as $(m^2\,W^{-1})$, which can be written as[70] $n' = n + \gamma I = n + \frac{n_2}{2}|E|^2$, where "n" is the linear refractive index, "I" denotes intensity, "E" is the strength of the applied optical field, and "n_2" gives the rate at which the refractive index is enhanced with increasing optical intensity. According to Sheik and Bahae, "n_2" and "γ" are interconvertible accordingly,[71]

$$\gamma(\mathrm{SI}) = \frac{n_2(\mathrm{esu})\,40\pi}{cn_o}. \tag{15}$$

Here, C is the speed of light and n_0 is the static linear refractive index. Figure 8(c) presents the dispersion of "γ" for these films. Here, the observed "γ" is 20–30 times greater than silica ($\gamma \sim 2.7 \times 10^{-20}\,m^2/W$) which signifies the potentiality of these laser-irradiated films for photonic devices.

Additionally, according to Mizrahi *et al.*,[72] non-linear absorption (β) also played an essential role in selecting optical materials for photonic applications. Reportedly, a high value of "β" eventually leads to a higher "n" and "γ," which diminishes the substantial limitations upon the applicability of non-linear optical materials. Thus, the non-linear absorption coefficient (β_c) can be calculated as follows:[73]

$$\beta_c(\nu) = \frac{3100\sqrt{21}\left[\left(\frac{2h\nu}{E_g}\right) - 1\right]^{\frac{3}{2}}}{n^2 E_g^3\left[\frac{2h\nu}{E_g}\right]^5}\,\mathrm{cm/GW}. \tag{16}$$

Figure 8(d) represents "β" as a function of incident photon energy. "β" primarily showed a much lower value, then with the increase in hν, "β" increases. Furthermore, the increase in lasing time results in a decreased pattern, which could be due to a change in the concentration of the defect. Both "β" and "γ" have been utilized to estimate the figure of merit (FOM), which played an essential role in effective non-linear device selection for improved device performance. Therefore, the expression of FOM is given by[71,74]

$$\mathrm{FOM} = \frac{2\beta\lambda}{\gamma}. \tag{17}$$

The estimated FOM in these films is in the order of 10^3 over the energy range of 0.7–1.12 eV. However, the requirement for the effective operation of a particular material as a device at a specific wavelength must be less than 1 (FOM < 1).[71]

c. Optical electronegativity. The ability of positive radicals of atoms to attract electrons of the same material to form ionic bonds is represented by optical electronegativity. Duffy evaluated optical electronegativity using the static refractive index as follows:[75] $\eta_{Opt} = \left(\frac{C}{n_o}\right)^{1/4}$, where "C" is a constant with a value of 25.54. In the non-linear media, "n" plays a very much important role in the electronic polarizability of ions and local fields inside the materials. This direct relation between "η_{Opt}" and "n" established an influential impact of "η_{Opt}" in the non-linear phenomenon. Table III shows that the estimated "η_{Opt}" values decrease with increasing lasing duration. Such inverse relation hints toward the change in the nature of bonding in the material with laser irradiation. This decrease is due to its inverse relationship with "n." The slight change in the η_{Opt} values could also be due to the covalent nature of the system.[27]

D. Surface wettability study

Surface wettability is an essential measurement of the liquid's ability to interact with the solid surface. It measures the level of wetting when the solid and liquid phases interact with each other. It contributes to the material's surface attributes and performs many essential tasks in printing and coating applications. This surface wettability is measured by a contact angle which is defined as the significance of free energy thermodynamic equilibrium within the solid–liquid–vapor phase. When the liquid droplet—here, water—is deposited on the solid surface as in Fig. 9(a), it will form a contact angle depending on the interfacial tension between liquid and vapor (γ_{WV}), solid and vapor (γ_{SV}), and the solid and liquid (γ_{SW}). Thus, according to Young's equation, $\gamma_{SV} = \gamma_{WV}\cos\theta_c + \gamma_{SW}$, where angle θ_c is formed by the solid surface and tangent of the droplet and is called the "contact angle."[76] The contact angle is an indicator of surface wettability and has been widely adopted in the industrial field as an evolution method of surfaces. A lower contact angle ($\theta \leq 90°$) signifies greater wettability (hydrophilic), whereas a higher contact angle ($\theta \geq 90°$) infers lower wettability (hydrophobic). Figures 9(b)–9(d) show one droplet of water (1 μl) over the surface of 0,30, and 90 min laser-irradiated thin films. It is clearly observed from Fig. 9 that the contact angle of all the presented films is lower than 90°, thus, these films have hydrophilic nature. The hydrophilic nature

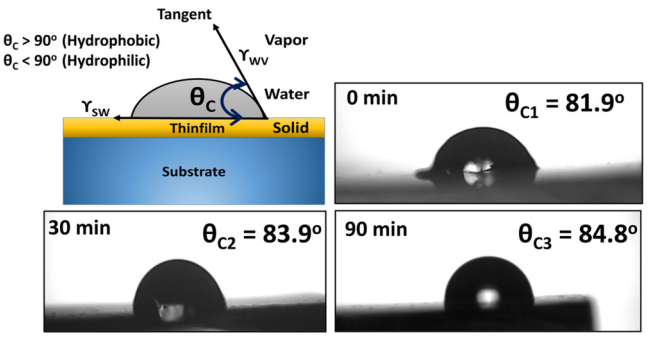

FIG. 9. (a) Schematic presentation of contact angle, water contact angle images of (b) 0, (c) 30, and (d) 90 min laser-irradiated $Bi_{15}In_{20}Se_{65}$ thin films.

observed in the 0 min irradiated film is greater (lower contact angle) than that of 30 and 90 min irradiated films. The difference in surface wettability might be due to the difference in the surface roughness of these films. Since the composition of all samples is identical, the effect of surface tension on these samples is negligible. Therefore, here, surface roughness plays a dominant role than surface tension in surface wettability determination. Furthermore, according to the Cassie–Baxter model, the significance of surface roughness over surface wettability can be explained by less air trapping between liquid and solid on the smooth surface compared to the rough one. Therefore, due to the hydrophilic nature of 0, 30, and 90 min laser-irradiated films, the water droplets spread more efficiently over a large surface area of the film, minimizing dust, dirt, and fouling accumulation on the surface. Moreover, the lower contact angle showed a larger surface area between solid and liquid, which depends on surface-free energy and surface morphology. Thereby, all the films could be used in various applications such as self-cleaning, antifouling, and antifogging as coating materials.[77] The hydrophilic nature of SnSe thin films having E_g of 0.9–1 eV increased with Se content and acts as a suitable material for coating.[77] The hydrophilicity observed in case of ion-irradiated Cu_2InSnS_4 thin films having a bandgap between 1.4 and 0.9 eV showed potential for photocatalysis and self-cleaning applications.[76] Similar hydrophilic behavior in the case of a $CdSe_{0.6}Te_{0.4}$ thin film having E_g 1.4 eV favors to enhance electrode/electrolyte interfacial contacts for better photoelectrochemical cells.[78]

The surface-free energy of the material defines the behavior of the surface and interface during the wetting and adhesion processes. The surface-free energy (γ) of different laser-irradiated films was calculated using the following expression:[79]

$$\gamma = \frac{\gamma_w\,(1+\cos\,\theta)^2}{4}, \tag{18}$$

where γ_w is the surface tension of water having a value of 71.99 mN/m. The estimated values of γ for all the films were 23.42, 22.02, and 21.40 mN/m, respectively. Similarly, surface adhesion is considered as another crucial parameter in the phenomenon of wetting the solid surface. By definition, adhesion signifies molecular attraction among the solid surfaces in contact. The binding strengths among the water droplets and the thin film surface were determined by the work of adhesion (W_{sl}), by using Young–Dupre's equation,[79] given by

$$W_{sl} = \gamma_w(1+\cos\,\theta), \tag{19}$$

where W_{sl} is the work of adhesion among the solid and liquid surfaces and γ_w is the liquid and air interfacial surface tension. The obtained W_{sl} for all the films was 82.13, 79.63, and 78.51 mN/m, respectively.

IV. CONCLUSION

The current work investigated changes in the optical, morphological, and structural properties of laser-irradiated $Bi_{15}In_{20}Se_{65}$ thin films with different irradiation times. The retention of the amorphous nature and smooth surface texture, even after laser irradiation, did not show much structural modification. The broad transparency and less absorption over the IR region make these films appealing for IR optics such as temperature detection, energy management, monitoring, night vision, etc. The films showed photodarkening behavior with irradiation time due to creating more defects and disorders over the band edge region by reducing E_g. Both the extinction coefficient and refractive index enhanced with the lasing duration, also indicating an increment in the scattering centers. The improvement in refractive indices has great significance in improving the optical intensity of the material and could possibly be used to design integrated circuits, IR sensors, ultrafast optical devices, etc. The real and imaginary dielectric constants enhanced with the lasing duration, while the tangential loss showed a reverse pattern. The increase in exposure duration enhances the interband transition, which might be due to the enhancement in the carrier concentration and the presence of more defect states with irradiation-induced bond breaking and rearrangements. The non-linear susceptibility and refractive index enhanced 9 times with the exposure time from 0 to 90 min. The non-linear absorption coefficient showed a higher magnitude with time, making these samples more appealing for non-linear device applications. The hydrophilic nature of the laser-irradiated films makes them possible for applications such as self-cleaning, antifouling, and antifogging as coating materials.

AUTHOR DECLARATIONS

Conflict of Interest

The authors have no conflicts to disclose.

Author Contributions

P. Priyadarshini: Data curation (equal); Investigation (equal); Methodology (equal); Writing – original draft (equal). **A. Parida:** Data curation (equal); Methodology (equal). **D. Alagarasan:** Data curation (equal); Investigation (equal). **R. Ganesan:** Data curation (equal); Investigation (equal). **R. Naik:** Conceptualization (lead); Investigation (lead); Supervision (lead); Writing – review & editing (lead).

DATA AVAILABILITY

The data that support the findings of this study are available from the corresponding author upon reasonable request.

REFERENCES

[1]J. Kim, M. Kang, W. Kim, J. Lee, C. Yoon, J. Joo, and H. Sohn, "Impact of Ag doping on subthreshold conduction in amorphous Ga_2Te_3 with threshold switching," J. Alloys Compd. **913**, 165176 (2022).
[2]P. Priyadarshini, D. Alagarsan, R. Ganesan, S. Varadharajaperumal, and R. Naik, "Influence of proton ion irradiation on the linear–nonlinear optoelectronic properties of $Sb_{40}Se_{20}S_{40}$ thin films at different fluences for photonic devices," ACS Appl. Opt. Mater. **1**, 55 (2023).
[3]Y. S. Obeng, N. V. Nguyen, P. K. Amoah, J. Ahn, M. Y. Shalaginov, J. Hu, and K. A. Richardson, "Dielectric spectroscopic investigation of reversible photo-induced changes in amorphous $Ge_2Sb_2Se_5$ thin films," J. Appl. Phys. **131**, 075102 (2022).
[4]S. Das, S. Senapati, D. Alagarsan, R. Ganesan, S. Varadharajaperumal, and R. Naik, "Thermal annealing-induced transformation of structural,

morphological, linear, and nonlinear optical parameters of quaternary $As_{20}Ag_{10}Te_{10}Se_{60}$ thin films for optical applications," ACS Appl. Opt. Mater. **1**, 17 (2023).
[5]P. Khan and K. V. Adarsh, "Light-induced effects in amorphous chalcogenide glasses: Femtoseconds to seconds," Physics **3**, 255–274 (2021).
[6]S. S. Ashraf, "Selenium-based amorphous semiconductors and their application in biomedicine," in *Electronic Devices, Circuits, and Systems for Biomedical Applications* (Academic Press, 2021), Chap. 2, pp. 25–46.
[7]T. Halenkovic, M. Kotrla, J. Gutwirth, V. Nazabal, and P. Nemec, "Insight into the photoinduced phenomena in ternary Ge-Sb-Se sputtered thin films," Photonics Res. **10**, 2261–2266 (2022).
[8]A. Kovalskiy, J. A. Allen, R. Golovchak, J. Oelgoetz, O. Shpotyuk, M. Vlcek, and K. Palka, "Parameterization of photobleaching and photodarkening *in-situ* kinetics in thermally deposited $GeSe_2$ thin films," Thin Solid Films **726**, 138659 (2021).
[9]Deepika, H. Singh, and N. S. Saxena, "Laser-induced optically modified $Se_{58}Ge_{27}Pb_{15}$ and $Se_{58}Ge_{24}Pb_{18}$ thin films, radiat," Eff. Defects **175**, 482–491 (2020).
[10]R. Naik, C. Sripan, and R. Ganesan, "Photo darkening in $As_{50}Se_{50}$ thin films by 532 nm laser irradiation," Opt. Laser Technol. **90**, 158–164 (2017).
[11]P. Priyadarshini, D. Sahoo, and R. Naik, "A review on the optical properties of some germanium-based chalcogenide thin films and their applications," Opt. Quantum Electron. **54**, 166 (2022).
[12]A. Aparimita, R. Naik, and R. Ganesan, "Laser-induced optical photobleaching in Bi-doped $Ge_{30}Se_{70}$ amorphous thin films," Appl. Phys. A **126**, 5 (2020).
[13]Deepika, M. Dixit, K. Kundu, and H. Singh, "Effect of 532 nm Nd:YAG laser irradiation on the optical properties of $Ge_1Se_{2.5}$ glass film," J. Mod. Opt. **68**, 868–877 (2021).
[14]L. Pan, B. Song, N. Mao, C. Xiao, C. Lin, P. Zhang, X. Shen, and S. Dai, "Optical properties of Ge-Sb-Se thin films induced by femtosecond laser," Opt. Commun. **496**, 127123 (2021).
[15]M. Behera, N. C. Mishra, and R. Naik, "Laser irradiation-induced structural, microstructural and optical properties change in Bi-doped $As_{40}Se_{60}$ thin films," Phase Transit. **93**, 148–157 (2020).
[16]S. Sharma, P. Kumar, and R. Thangaraj, "Effect of Bi additive on structure and optical properties of amorphous $Bi_xIn_{25-x}Se_{75}$ chalcogenide films," Curr. Appl. Phys. **13**, 731–735 (2013).
[17]S. W. Chen, Y. Hutabalian, W. Gierlotka, C. H. Wang, and S. T. Lu, "Phase diagram of Bi–In–Se ternary system," Calphad **68**, 101744 (2020).
[18]R. P. Tripathi, M. Zulfequar, and S. A. Khan, "Thickness dependent structural, optical and electrical properties of $Se_{85}In_{12}Bi_3$ nanochalcogenide thin films," Mater. Res. Express **5**, 046409 (2018).
[19]P. Priyadarshini, S. Das, D. Alagarasan, R. Ganesan, S. Varadharajaperumal, and R. Naik, "Role of bismuth incorporation on the structural and optical properties in $Bi_xIn_{35-x}Se_{65}$ thin films for photonic applications," J. Am. Ceram. Soc. **104**, 5803–5814 (2021).
[20]P. Priyadarshini, D. Sahoo, D. Alagarasan, R. Ganesan, S. Varadharajaperumal, and R. Naik, "Phase transformation induced linear and nonlinear properties change in Bi/In_2Se_3 films upon annealing and irradiation for optoelectronic applications," J. Appl. Phys. **129**, 223101 (2021).
[21]M. M. Soraya, "Structural and optical properties of $Se_{85-x}Te_{15}In_x$ chalcogenide thin films for optoelectronics," Appl. Phys. A **126**, 590 (2020).
[22]Y. Liu, L. Cao, J. Zhong, J. Yu, J. He, and Z. Liu, "Synthesis of bismuth selenide nanoplates by solvothermal methods and its stacking optical properties," J. Appl. Phys. **125**, 035302 (2019).
[23]K. H. Harbbi and S. S. Jahil, "Study the lattice distortion and particle size of one phase of MnO by using Fourier analysis of x-ray diffraction lines," Adv. Phys. Theories Appl. **65**, 6–22 (2017).
[24]L. A. Walsh, C. M. Smyth, A. T. Barton, Q. Wang, Z. Che, R. Yue, J. Kim, M. J. Kim, R. M. Wallace, and C. L. Hinkle, "Interface chemistry of contact metals and ferromagnets on the topological insulator Bi_2Se_3," J. Phys. Chem. C **121**, 23551–23563 (2017).
[25]M. Kim, D. J. Kim, D. Ha, and T. Kim, "Cracking-assisted fabrication of nanoscale patterns for micro/nanotechnological applications," Nanoscale **8**, 9461–9479 (2016).
[26]A. S. Hassanien, "Intensive linear and nonlinear optical studies of thermally evaporated amorphous thin Cu-Ge-Se-Te films," J. Non-Cryst. Solids **586**, 121563 (2022).
[27]S. K. Sahoo, S. Mangal, D. K. Mishra, P. Kumar, and U. P. Singh, "Effect of low energy proton beam irradiation on structural and electrical properties of ZnO:Al thin films," Mater. Sci. Semicond. Proc. **63**, 76–82 (2017).
[28]E. R. Shaaban, "Optical constants and fitted transmittance spectra of varies thickness of polycrystalline ZnSe thin films in terms of spectroscopic ellipsometry," J. Alloys Compd. **563**, 274–279 (2013).
[29]S. Mishra, P. L. Singh, and D. K. Dwivedi, "Thin film preparation and optical properties of Se–Te based chalcogenide glasses for optoelectronic applications," Glass Phys. Chem. **46**, 341–349 (2020).
[30]F. Charpentier, B. Bureau, J. Troles, C. Boussard-Plédel, K. Michelle-Le Pierres, F. Smektala, and J. L. Adam, "Infrared monitoring of underground CO_2 storage using chalcogenide glass fibers," Opt. Mater. **31**, 496–500 (2009).
[31]H. I. Elsaeedy, A. Qasem, M. Mahmoud, H. A. Yakout, and S. A. Abdelaal, "The precise role of UV exposure time in controlling the orbital transition energies, optical and electrical parameters of thermally vacuum evaporated $Se_{50}Te_{50}$ thin film," Opt. Mater. **115**, 111053 (2021).
[32]Z. H. Khan, S. A. Khan, N. Salah, S. Habib, S. M. Abdallah El-Hamidy, and A. A. Al-Ghamdi, "Effect of composition on electrical and optical properties of thin films of amorphous Ga_xSe_{100-x} nanorods," Nanoscale Res. Lett. **5**, 1512–1517 (2010).
[33]M. Behera, N. C. Mishra, R. Naik, C. Sripan, and R. Ganesan, "Thermal annealing induced structural, optical and electrical properties change in $As_{40}Se_{60-x}Bi_x$ chalcogenide thin films," AIP Adv. **9**, 095065 (2019).
[34]S. N. Moger, D. U. Shanubhogue, R. Keshav, and M. G. Mahesha, "Spectroscopic and electrical analysis of vacuum co-evaporated $Cd_xZn_{1-x}Te$ thin film," Superlattices Microstruct. **142**, 106521 (2020).
[35]Z. A. Alrowaili, M. M. Soraya, T. A. Alsultani, A. Qasem, E. R. Shaaban, and M. Ezzeldien, "Sn-induced changes in the structure and optical properties of amorphous As–Se–Sn thin films for optical devices," Appl. Phys. A **127**, 1–11 (2021).
[36]S. N. Moger, V. Sathe, and M. G. Mahesha, "Characterization of ZnS_xSe_{1-x} films grown by thermal co-evaporation technique for photodetector applications," Surf. Interfaces **30**, 101852 (2022).
[37]A. S. Hassanien, I. Sharma, and P. Sharma, "Inference of Sn addition on optical properties of the novel thermally evaporated thin a-$Ge_{15}Te_{50}S_{35-x}Sn_x$ films and some physical properties of their glasses," Mater. Chem. Phys. **293**, 126887 (2023).
[38]L. W. Benjamin, P. Dube, C. B. Tabi, and C. M. Muiva, "Physical, linear and nonlinear optical properties of amorphous $Se_{90-x}Te_{10}M_x$ (M = Zn, In, Pb, x = 0, 5) chalcogenide thin films by electron-beam deposition," J. Non-Cryst. Solids **557**, 120646 (2021).
[39]A. El-Denglawey, K. A. Aly, A. Dahshan, and A. S. Hassanien, "Optical characteristics of thermally evaporated thin a-$(Cu_2ZnGe)_{50-x}Se_{50+x}$ films," ECS J. Solid State Sci. Technol. **11**, 044006 (2022).
[40]E. A. Davis and N. F. Mott, "Conduction in non-crystalline systems V conductivity, optical absorption and photoconductivity in amorphous semiconductors," Philos. Mag. **22**, 903–922 (1970).
[41]R. Naik, N. Behera, and R. Ganesan, "Laser induced optical photo darkening in $Sb_{30}S_{40}Se_{30}$ chalcogenide thin films," Adv. Sci. Lett. **20**, 559–564 (2014).
[42]F. A. Al-Agel, "Optical properties of thin films of $Ga_{15}Se_{75}Ag_{10}$ chalcogenide glasses before and after laser irradiation," Sci. Adv. Mat. **3**, 245–250 (2011).
[43]M. Behera, S. Behera, and R. Naik, "Optical band gap tuning by laser induced Bi diffusion into As_2Se_3 film probed by spectroscopic techniques," RSC Adv. **7**, 18428–18437 (2017).
[44]D. Alagarasan, S. Varadharajaperumal, D. A. Kumar, R. Naik, S. Umrao, M. Shkir, S. AlFaify, and R. Ganesan, "Influence of nanostructured SnS thin films for visible light photo detection," Opt. Mater. **121**, 111489 (2021).
[45]A. Qasem, M. S. Mostafa, H. A. Yakout, M. Mahmoud, and E. R. Shaaban, "Determination of optical bandgap energy and optical characteristics of $Cd_{30}Se_{50}S_{20}$ thin film at various thicknesses," Opt. Laser Technol. **148**, 107770 (2022).

[46]A. S. Hassanien, H. R. Alamri, and I. M. El Radaf, "Impact of film thickness on optical properties and optoelectrical parameters of novel $CuGaGeSe_4$ thin films synthesized by electron beam deposition," Opt. Quantum Electron. **52**, 335 (2020).
[47]E. R. Shaaban, M. Y. Hassaan, M. G. Moustafa, A. Qasem, G. A. M. Ali, and E. S. Yousef, "Optical constants, dispersion parameters and non-linearity of different thickness of $As_{40}S_{45}Se_{15}$ thin films for optoelectronic applications," Optik **186**, 275–287 (2019).
[48]A. S. Hassanien and I. Sharma, "Dielectric properties, optoelectrical parameters and electronic polarizability of thermally evaporated a-Pb-Se-Ge thin films," Physica B **622**, 413330 (2021).
[49]D. Sahoo, P. Priyadarshini, R. Dandela, D. Alagarasan, R. Ganesan, S. Varadharajaperumal, and R. Naik, "*In situ* laser irradiation: The kinetics of the changes in the nonlinear/linear optical parameters of $As_{50}Se_{40}Sb_{10}$ thin films for photonic applications," RSC Adv. **11**, 16015–16025 (2021).
[50]I. Sharma, P. Sharma, and A. S. Hassanien, "Optical properties and optoelectrical parameters of the quaternary chalcogenide amorphous $Ge_{15}Sn_xS_{35-x}Te_{50}$ films," J. Non-Cryst. Solids **590**, 121673 (2022).
[51]T. S. Moss, "A relationship between the refractive index and the infra-red threshold of sensitivity for photoconductors," Proc. Phys. Soc. B **63**, 167–176 (1950).
[52]P. Singh and R. Kumar, "Investigation of refractive index dispersion parameters of Er doped ZnO thin films by WDD model," Optik **246**, 167829 (2021).
[53]S. Mishra, P. Kumar Singh, R. K. Yadav, A. Umar, P. Lohia, and D. K. Dwivedi, "Investigation of glass forming ability, linear and non-linear optical properties of Ge-Se-Te-Sb thin films," Chem. Phys. **541**, 111021 (2021).
[54]K. Tanaka, "Optical properties and photoinduced changes in amorphous As-S films," Thin Solid Films **66**, 271–279 (1980).
[55]R. Y. Petrus, H. A. Ilchuk, A. I. Kashuba, I. V. Semkiv, E. O. Zmiiovska, and F. M. Honchar, "Optical properties of CdS thin films," J. Appl. Spectrosc. **87**, 35–40 (2020).
[56]A. S. Hassanien, K. A. Aly, H. I. Elsaeedy, and A. Alqahtani, "Optical characterization and dispersion discussions of the novel thermally evaporated thin $a\text{-}S_{50-x}Ge_{10}Cd_xTe_{40}$ films," Appl. Phys. A **128**, 1021 (2022).
[57]Ambika and P. B. Barman, "An optical study of vacuum evaporated $Se_{85-x}Te_{15}Bi_x$ chalcogenide thin films," Physica B **405**, 822–827 (2010).
[58]S. Sharda, E. Sharma, K. A. Aly, A. Dahshan, and P. Sharma, "High refractive index (Dy) doped $(GeTe_2)_{80}(In_2Te_3)_{20}$ thin films for sub-THz and millimeter-wave applications," Ceram. Int. **47**, 34501–34507 (2021).
[59]M. Alzaid, A. Qasem, E. R. Shaaban, and N. M. A. Hadia, "Extraction of thickness, linear and nonlinear optical parameters of $Ge_{20+x}Se_{80-x}$ thin films at normal and slightly inclined light for optoelectronic devices," Opt. Mater. **110**, 110539 (2020).
[60]R. Sharma, S. Sharda, and K. A. Aly, "Nano-crystallization and optical properties of quaternary Sn–Se–Bi–Te chalcogenide thin films," J. Mater. Sci Mater. Electron. **33**, 16320–16333 (2022).
[61]A. Hassanien, K. Aly, and A. Akl, "Study of optical properties of thermally evaporated ZnSe thin films annealed at different pulsed laser powers," J. Alloys Compd. **685**, 733–742 (2016).
[62]G. Nagpal, I. Sharma, and S. Tripathi, "The effect of the substitution of Sb with Zn on the optical and physical properties of $Se_{90}Sb_{10-x}Zn_x$ (x = 0, 2, 4, 6, 10 at. %) thin films," Opt. Int. J. Light Electron Opt. **207**, 164460 (2020).
[63]S. Singh and N. Singh, "Nonlinear effects in optical fibers, origin, management and applications," Prog. Electromag. Res., PIER **73**, 249–275 (2007).
[64]H. Titcha and L. Titchy, "Semiempirical relation between non-linear suscrptibility (refractive index), linear refractive index and optical gap and its application to amorphous chalcogenides," J. Optoelectron. Adv. Mater. **4**, 381–386 (2002).
[65]M. Frumar, J. Jedelsky, B. Frumarova, T. Wagner, and M. Hrdlicka, "Optically and thermally induced changes of structure, linear and nonlinear optical properties of chalcogenides thin films," J. Non-Cryst. Solids **399**, 326–327 (2003).
[66]K. Anshu and A. Sharma, "Study of Se based quaternary Se-Pb-(Bi,Te) chalcogenide thin films for their linear and nonlinear optical properties," Optik **127**, 48–54 (2016).
[67]P. Priyadarshini, S. Das, D. Alagarasan, R. Ganesan, S. Vardharajperumal, and R. Naik, "Observation of high nonlinearity in Bi doped $Bi_xIn_{35-x}Se_{65}$ thin films with annealing," Sci. Rep. **11**, 21518 (2021).
[68]A. A. A. Darwish and H. A. M. Ali, "On annealing induced effect in optical properties of amorphous GeSeSn chalcogenide films for optoelectronic applications," J. Alloys Compd. **710**, 431–435 (2017).
[69]M. Dongol, A. F. Elhady, M. S. Ebied, and A. A. Abuelwafa, "Effect of thermal annealing on the optical properties of $Ge_{20}Se_{65}S_{15}$ thin films," Indian J. Phys. **95**, 1245–1253 (2021).
[70]A. Alizadeh, Y. Rajabi, and M. M. Bagheri–Mohagheghi, "Effect of crystallinity on the nonlinear optical properties of indium–tin oxide thin films," Opt. Mater. **131**, 112589 (2022).
[71]J. Tasseva, R. Todorov, T. Babeva, and K. Petkov, "Structural and optical characterization of Ag photo-doped thin $As_{40}S_{60-x}Se_x$ films for nonlinear applications," J. Opt. **12**, 065601 (2010).
[72]V. Mizrahi, K. W. Delong, G. I. Stegeman, M. A. Saifi, and M. J. Andrejco, "Two-photon absorption as a limitation to all-optical switching," Opt. Lett. **14**, 1140 (1989).
[73]A. A. Abuelwafa, M. S. Abd El-Sadek, S. Elnobi, and T. Soga, "Effect of transparent conducting substrates on the structure and optical properties of tin (II) oxide (SnO) thin films: Comparative study," Ceram. Int. **47**, 13510–13518 (2021).
[74]A. Kumar, S. Shukla, and R. K. Shukla, "Evaluation of nonlinear optical parameters of $Se_{40}As_{60-x}S_x$ (x = 10, 20) chalcogenide thin films for photonic applications," Indian J. Phys. (published online 2022).
[75]J. A. Duffy, "Trends in energy gaps of binary compounds: An approach based upon electron transfer parameters from optical spectroscopy," J. Phys. C Solid State Phys. **13**, 2979 (1980).
[76]C. Nefzi, B. Yahmadi, N. E. Guesmi, J. M. Garcia, N. Kamoun-Turki, and S. A. Ahmed, "A successful exploitation of gamma-radiation on chalcogenide Cu_2InSnS_4 towards clean water under photocatalysis approach," J. Mol. Struct. **1251**, 131943 (2022).
[77]D. Kim, J. Park, J. Choi, J. W. Oh, and Y. C. Kang, "Compositional ratio effect on the physicochemical properties of SnSe thin films," Physica B **612**, 412890 (2021).
[78]S. K. Shinde, D. P. Dubal, G. S. Ghodake, and V. J. Fulari, "Synthesis and characterization of chemically deposited flower-like $CdSe_{0.6}Te_{0.4}$ thin films for solar cell application," Mater. Lett. **126**, 17–19 (2014).
[79]A. B. Gurav, S. S. Latthe, R. S. Vhatkar, J. G. Lee, D. Y. Kim, J. J. Park, and S. S. Yoon, "Superhydrophobic surface decorated with vertical ZnO nanorods modified by stearic acid," Ceram. Int. **40**, 7151–7160 (2014).